Computational modelling identifies key determinants of subregion-specific dopamine dynamics in the striatum

Aske L. Ejdrup[1,†], Jakob K. Dreyer[2], Matthew D. Lycas[1], Søren H. Jørgensen[1], Trevor W. Robbins[3,4], Jeffrey W. Dalley[3,4,5], Freja Herborg[1, †, *], Ulrik Gether[1, †, *]

[1]Department of Neuroscience, Faculty of Health and Medical Sciences, Maersk Tower 7.5, University of Copenhagen, DK-2200 Copenhagen, Denmark

[2]Department of Bioinformatics, H Lundbeck A/S, Valby, Denmark

[3]Behavioural and Clinical Neuroscience Institute, University of Cambridge, Cambridge CB2 3EB, UK

[4]Department of Psychology, University of Cambridge, Cambridge CB2 3EB, UK

[5]Department of Psychiatry, University of Cambridge, Cambridge CB2 0SZ, UK

*These authors contributed equally to the work

†To whom correspondence should be addressed: ejdrup@sund.ku.dk, frejahh@sund.ku.dk or gether@sund.ku.dk

Abstract

Striatal dopamine (DA) release regulates reward-related learning and motivation and is believed to consist of a short-lived *phasic* and continuous *tonic* component. Here, we build a large-scale three-dimensional model of extracellular DA dynamics in dorsal (DS) and ventral striatum (VS). The model predicts rapid dynamics in DS with little-to-no basal DA, and slower dynamics in the VS enabling build-up of *tonic* DA levels. These regional differences do not reflect release-related phenomena but rather differential dopamine transporter (DAT) activity. Interestingly, our simulations posit DAT nanoclustering as a possible regulator of this activity. Receptor binding simulations show that D1 receptor occupancy follows extracellular DA concentration with milliseconds delay, while D2 receptors do not respond to brief pauses in firing but rather integrate DA signal over seconds. Summarized, our model distills recent experimental observations into a computational framework that challenge prevailing paradigms of striatal DA signalling.

Introduction

Striatal dopamine (DA) release is essential for regulating reward-related learning, incentive motivation, and motor function *(Berke, 2018; Klaus et al, 2019)*. DA exerts these roles over a broad range of time scales, yet DA primarily operates as a volume transmitter that targets metabotropic receptors located within a micrometre range from the sites of release *(Agnati et al, 1995; Borroto-Escuela et al, 2018; Cragg & Rice, 2004; Gonon et al, 2000; Sulzer et al, 2016)*. The temporal and spatial dynamics of DA release in striatum, however, remain a highly contested topic. Classically, DA release has been divided into *tonic* release, driven by pacemaker-like spontaneous firing, and *phasic* release from coordinated bursts of firing across neurons *(Niv et al, 2007; Schultz, 2007; Sulzer et al., 2016)*. However, this sharp distinction in release modes, as well as the existence of a basal DA level has recently been challenged *(Berke, 2018; Ejdrup et al, 2023; Jorgensen et al, 2023; Liu et al, 2021; Sippy & Tritsch, 2023)*.

The picture is further complicated by major regional differences across striatal sub domains. These include differences in Ca^{2+}-channel and nicotinic acetylcholine receptor (nAChR) expression profiles on DA terminals, as well differential regulation and expression of the DA transporter (DAT) *(Brown et al, 2011; Cardozo & Bean, 1995; Kearney et al, 2023; Richards & Zahniser, 2009; Threlfell et al, 2010)*. In addition, we and others have found remarkable differences in extracellular DA release dynamics between the dorsal (DS) and ventral striatum (VS) *(Jorgensen et al., 2023; Mohebi et al, 2024; Salinas et al, 2023)*. Fibre photometry recordings in the DS in mice using the DA sensor dLight1.3b during self-paced exploratory activity showed a rapidly fluctuating signal, whereas we observed up to minutes-long DA dynamics in VS that correlated with behavioural output *(Jorgensen et al.,*

2023). Concurrent measurements of extracellular DA by microdialysis and fibre photometry have furthermore corroborated the lack of tonic levels of DA in DS while supported its presence in VS *(Ejdrup et al., 2023; Jorgensen et al., 2023)*. Despite these reported differences in striatal DA dynamics, electrophysiological recordings suggest that DA neurons from the primary innervators of DS, substantia nigra par compacta (SNc) and VS, ventral tegmental area (VTA), have remarkably similar firing patterns at rest *(Dodson et al, 2016)*. We therefore set out to better understand the fundamental principles governing extracellular DA dynamics by constructing a new computational model of the striatal DA system.

Extracellular DA dynamics have been modelled before; either one-dimensionally or with a primary focus on single release events or post-synaptic receptor binding *(Beyene et al, 2017; Dreyer et al, 2010; Dreyer & Hounsgaard, 2013; Dreyer et al, 2016; Venton et al, 2003; Wiencke et al, 2020)*. Here, we present a three-dimensional model of tens of thousands of release sites, focused on larger-scale signalling and based on experimentally observed biological parameters. The model faithfully replicates experimentally observed results as well as the difference in DA dynamics between DS and VS. Importantly, it offers compelling evidence that these differences do not primarily reflect different release phenomena but rather arise from differential expression and possibly nanoscale localization of the DA transporter (DAT).

Results

Construction of a model of DA dynamics in the striatum

We constructed a novel model of DA release using experimentally determined parameters from DS, including release, uptake, and cytoarchitecture *(Doucet et al, 1986; Dreyer et al., 2010; Dreyer & Hounsgaard, 2013; Liu et al., 2021; Olson et al, 1972; Sulzer et al., 2016)*. DA release sites on axons projecting from the midbrain were randomly simulated as uniformly distributed discrete points in a three-dimensional space (Figure 1A). The release events themselves were simulated as point source events *(Cragg & Rice, 2004)* driven by action potentials (AP). We then modelled DA release for each voxel in the simulation containing a release site as function of three key parameters; firing rate, release probability and quantal size:

(1)

$$\mathrm{release}_{\mathrm{n,t}} = \mathrm{Poisson}(\mathrm{f}_{\mathrm{rate}}\ \mathrm{dt})_{\mathrm{n}}\ \mathrm{P}(\mathrm{R}_{\%})_{\mathrm{t}}\ \mathrm{Q}\ \mathrm{dt}$$

where $\mathrm{Poisson}(\mathrm{f}_{\mathrm{rate}}\ \mathrm{dt})_{\mathrm{n}}$ is a Poisson distribution of action potentials (AP) for the given neuron (n) with the firing rate $\mathrm{f}_{\mathrm{rate}}(I)$, $\mathrm{P}(\mathrm{R}_{\%})_{\mathrm{t}}$ is the probability of release at the individual terminal (t) for each AP, while Q is the number of DA molecules released per event (dopaminergic quantal size) and dt the time step. Changing $\mathrm{f}_{\mathrm{rate}}$ can be used to model both pacemaker firing, typically reported at 2-10 Hz, and burst firing, which can exceed 20 Hz *(Sulzer et al., 2016)*.

DA reuptake in the striatum is almost exclusively mediated by the DA transporter (DAT) *(Jones et al, 1998)*, which is widely distributed along DA axons and varicosities *(Block et al, 2015; Eriksen et al, 2010; Eriksen et al, 2009)*. As reuptake follows concentration-dependent Michaelis-Menten kinetics *(Nicholson, 1995)*, we simulated uptake as follows:

(2)

$$\text{uptake} = \frac{V_{max}\ [DA]}{K_m\ +\ [DA]}\ dt$$

where $[DA]$ is the concentration of DA for each voxel in the model, V_{max} is the maximal uptake capacity in the region and K_m is the concentration of DA at which half of V_{max} is reached.

The spatial distribution of released DA is a complex interplay between release, uptake and diffusion. Diffusion in an open 3D space can be simulated for each voxel with a Laplacian operator:

(3)

$$\text{diffusion} = \frac{\partial DA_{x,y,z,t}}{\partial t} = D_a\ dt\left(\frac{\partial^2 DA_{x,y,z,t}}{\partial x^2} + \frac{\partial^2 DA_{x,y,z,t}}{\partial y^2} + \frac{\partial^2 DA_{x,y,z,t}}{\partial z^2}\right)$$

where D_a is a corrected diffusion coefficient and *dt* is the timestep. As the extracellular space of the striatum is tortuous, we modified the conventional diffusion coefficient D to an apparent diffusion coefficient (D_a) to correct for the tortuosity (λ) of the striatum *(Cragg & Rice, 2004; Nicholson, 1985)*:

(4)

$$D_a = \frac{D}{\lambda^2}$$

As the cerebellum exhibits as tortuosity to that recorded in the striatum, we assumed a uniform tortuosity throughout the striatum *(Nicholson & Phillips, 1981)*. Combining equation 1 through 4, we model DA changes in each voxel with a single conceptual equation:

(5)

$$\frac{dDA}{dt} = \text{release} - \text{uptake} + \text{diffusion}$$

We first compared our 3D model of DA dynamics to the analytical solution of a single release event *(Cragg & Rice, 2004; Gonon et al., 2000)*. To do this, we simulated a quantal event of 3000 DA molecules and calculated DA concentrations across space at three separate time points (Figure 1B, C). The analytic solution and our model predicted almost identical results. Slight differences were introduced as the analytical solution assumes linear uptake from DAT while our model incorporate non-linear Michaelis-Menten kinetics. These differences, however, were almost negligible. The main difference between the two models lies in scalability across both space and time. Summarized, the model enables a dynamic incorporation of the surrounding DA concentration, release events and uptake, and can be scaled to cover DA dynamics of a large 3D space, whose size and granularity is only limited by computing power (see Code Availability Section for the Python code with numerical implementations of the equations listed and scripts to run the simulations and plot the main figures).

We also tested the validity of our model, by examining the response to electrical stimulation. Importantly, our model faithfully mirrored DA release seen with fast-scan cyclic voltammetry (FSCV) recordings upon direct stimulation of striatal slices when we corrected for kinetics of the typical FSCV recording setup (Figure S1b, c and discussion in Supplementary Information) *(Atcherley et al, 2015; Brimblecombe et al, 2019; Stuber et al, 2010; Xie et al, 2020)*.

Simulating large scale DA dynamics of the dorsal striatum

To better understand the extracellular DA dynamics that arise from the balance between dopaminergic pacemaker activity and uptake, we simulated DA dynamics in the DS generated by pacemaker activity (4 Hz) of 150 neurons in the midbrain in a 100x100x100 µm

128 space (Figure 1D, see parameters in Table 1). Our simulations yielded a pattern of partially
129 segregated DA hot spots with large fractions of the simulated space devoid of DA,
130 suggesting that release events in DS only elevate DA in the immediate surroundings with
131 DAT-dependent clearance preventing a larger spread in space (Figure 1D and Video 1). This
132 was also illustrated by a cross-section in time (Figure 1E). In line with our recent in vivo
133 microdialysis experiments, the average DA concentration in the simulations during
134 pacemaker activity was approximately 10 nM *(Ejdrup et al., 2023)*. Further, when we
135 calculated the average concentration of a larger area across time, which fibre photometry
136 conceivably does, the results resembled a tonic DA concentration (Figure S1A). However,
137 our model predicted a spatial distribution that is highly heterogenous and devoid of
138 pervasive resting or tonic DA levels (Figure 1D-F).

139 To ensure our simulations were performed within a sufficiently large space to yield
140 consistent results, we tested different sizes of the simulated area and found a diameter of
141 50 μm to faithfully mimic the results of larger simulations (Figure S2A, B). Additionally, we
142 tested our simulations at different granularity (0.1, 0.5, 1 and 2 μm). The finer the spatial
143 grain, the higher detail close to a release event; however, at a spatial granularity of 1 μm,
144 [DA] deviated by <2% across most percentiles and only by >1 nM above the 99.5th percentile
145 (Figure S2C-F), leading us to use this voxel size for our simulations.

146

147 ## Burst firing and receptor occupancy

148 DA neurons are known to fire short bursts of APs, which is a phenomenon strongly linked to
149 reward-prediction error and learning *(Schultz, 2007)*. These bursts can also be induced
150 locally in the striatum by nicotinic receptor activation *(Liu et al, 2022; Matityahu et al,*
151 *2023)*.. To gain insights into extracellular DA dynamics following a locally induced burst, we

152 simulated three different firing scenarios for a group of terminals within a 10x10x10 µm
153 field encompassing roughly 40 release sites from the randomly simulated 150 neurons: 3
154 pulses at 10 Hz, 6 pulses at 20 Hz and 12 pulses at 40 Hz (Figure 1G – burst properties
155 matched to be the same duration). The middle scenario most closely resembles the
156 physiological burst behaviour reported in the literature, whereas the high-activity burst is
157 above what is typically seen. Unsurprisingly, peak DA concentration was reached at the end
158 of the bursts (Figure 1G). The 3 APs/10 Hz bursting scenario generated no significant spill-
159 over of DA outside the region of activity, whereas the 6 APs/20 Hz and 12 APs/40 Hz
160 bursting scenarios markedly overwhelmed uptake (Figure 1G). The relationship between
161 firing rate and the sphere of influence by DA became further evident when plotting maximal
162 concentration of the surrounding space (Figure S1D) and the volume of space with a DA
163 concentration above 100 nM (Figure S1E). We found that the 3 APs/10 Hz stimulation
164 produced DA responses that largely resembled that of a single pulse. In both cases, DA was
165 mostly cleared after 100 ms and the volume exposed to greater than 100 nM was similar
166 (Figure 1G and Figure S1E). In contrast, the high bursting activities caused a frequency-
167 dependent spill-over, where the areas exposed to a DA concentration above 100 nM were
168 10 and 30 times larger than the terminal origin for 6 APs/20 Hz and 12 APs/40 Hz,
169 respectively. Even after 100 ms, a considerable amount of DA remained in the 12 APs/40 Hz
170 scenario (Figure 1G).

171 To understand how these DA dynamics could affect the postsynaptic response, we
172 modelled receptor binding. D1 receptors (-Rs) were assumed to have a half maximal
173 effective concentration (EC_{50}) of 1000 nM, and we extrapolated the reverse rate constant
174 (k_{off}) to 19.5 s^{-1} based on a linear fit of the recently characterized DA receptor-based sensors
175 (Figure S1E) *(Labouesse & Patriarchi, 2021)*. We set the EC_{50} of D2Rs to 7 nM and k_{off} to 0.2

176 s^{-1} based on the DA sensor kinetic fit (Figure S1F), which matches a recent binding study
177 (0.197 s^{-1} for binding study vs. 0.204 s^{-1} based on linear fit), indicating the receptor-based
178 sensor fit can be extrapolated to the endogenous receptors *(Agren et al, 2021)*.. To
179 determine how these receptors would respond to our predicted DA dynamics, we simulated
180 pacemaker activity at 4 Hz with an added burst of 6 APs/20 Hz. Figure 1H shows a
181 representative trace of DA concentration and occupancy of the D1R and D2R for a voxel
182 with a release site. During pacemaker activity, D1R showed an occupancy close to 0,
183 whereas D2R occupancy was approximately 0.55 (Figure 1H). Both D1Rs and D2Rs
184 occupancies were due to a high diffusion rate mostly invariant to individual release events
185 caused by pacemaker activity. However, upon coordinated burst firing the occupancy
186 rapidly increased (Figure 1H and Video 2) as diffusion no longer equilibrates the
187 extracellular concentrations on a timescale faster than the receptors. D1R receptor
188 occupancy closely tracked extracellular DA with a delay of only ~50 ms for the typically
189 reported affinity of 1 µM (Figure 1I). By contrast, it took at least 5 seconds before the burst-
190 induced increase in D2R occupancy had declined to baseline levels (Figure 1H and Video 2).
191 This made the D2R incapable of temporally separating closely linked bursts of activity and
192 rather summarized the output, whereas the D1R occupancy reset between each individual
193 burst (Figure S1G). Perhaps more surprisingly, the D2R occupancy only fell from
194 approximately 0.55 to 0.45 when simulating a full second pause in firing due to the slow off
195 kinetics (Figure 1J). Indeed, this finding was robust across an order of magnitude of D2R
196 affinity (2 nm - 20 nM), although the sensitivity to a one-second pause was larger at an
197 affinity of 20 nM (Figure S1H).
198 These simulations suggest that the dopaminergic architecture of the DS limits DA
199 overflow during physiologically relevant bursting activity. Further, DA receptors had a

200 temporally mostly uniform response to DA release caused by pacemaker activity with D1R
201 occupancy responding rapidly to both onset and offset extracellular DA concentrations
202 following bursts, while D2R showed seconds-long delays in offset.
203

204 ## Ventral striatum maintains pervasive DA tone

205 Mounting evidence points to considerable differences in DA dynamics across striatal
206 subregions *(Jorgensen et al., 2023; Mohebi et al., 2024)*, which might reflect differences in
207 the cytoarchitectural and/or molecular dopaminergic make up. In line with this, most
208 studies report lower dopaminergic density in the VS than in DS regardless of methodological
209 modality with a median value of ~90% in VS relative to DS (Table S1). Further, DAT-mediated
210 uptake capacity is reported to be lower in VS with a median capacity at ~30% of DS (Table
211 S2). Consistently, we observed a clear dorsoventral gradient for DAT expression when
212 analysing immunostainings in striatal mouse brain slices from a previous publication
213 *(Sorensen et al, 2021)*(Figure S3A, B). By contrast, the VMAT2 staining only decreased
214 slightly from VS to DS (Figure S3A-C).

215 We simulated DA release during pacemaker activity in both DS and VS. DS values
216 were set as previously described (25 μm^3 per terminal, uptake capacity of 6.0 $\mu M\ s^{-1}$), but
217 for VS we reduced the terminal density to 90% (27.8 μm^3 per terminal) and DAT uptake
218 capacity to 33% (2.0 $\mu M\ s^{-1}$) (Tables S1 and S2). The remaining parameters were kept
219 identical. With these two differences, our simulations revealed markedly different
220 spatiotemporal DA distributions during pacemaker activity. While DS formed segregated
221 domains with low DA concentrations in the inter-domain space (Figure 2A and Video 1), DA
222 diffused further throughout the simulated space in VS, before being cleared by DAT. This
223 gave rise to what may be considered a tonic DA level with hotspots of higher DA

224 concentrations, although the concentration distribution is continuous (Figure 2A-C and
225 Video 1).
226 We compared our model of the two regions with existing experimental data. In an
227 earlier study by May and Wightman, 120 stimulus pulses were delivered in the medial
228 forebrain bundle (MFB) at either 10, 30 or 60 Hz and DA responses were recorded by FSCV
229 in both caudate-putamen (CPu) and nucleus accumbens (Nac) *(May & Wightman, 1989)*. To
230 mirror this, we simulated 120 action potentials at similar frequencies (10, 30, and 60 Hz) at
231 6% release probability and ran the result through convolution, as in Figure S1B and C, to
232 generate an FSCV read-out (Figure 2E). Since May and Wightman reported no significant
233 difference in DA released per electrically delivered pulse ($[DA]_p$) between VS and DS, we
234 applied equal quantal size and $R_{\%}$ for DS and VS in our simulations, while uptake capacity in
235 VS was kept to a third of DS and terminal density was set to 90% as specified above.
236 Importantly, our simulated FSCV data closely resembled the earlier findings, with VS
237 reaching considerably higher DA levels for all three stimulation frequencies (Figure 2E – see
238 *(May & Wightman, 1989)*). This regional difference presumably arises from differences in
239 DAT capacity between DS and VS, as the lower terminal density in VS would have the
240 opposite effect (see below) and the remaining parameters were held identical.
241 To compare with our results for DS, we tested how VS responded during simulated
242 burst activity. Using firing patterns identical to the DS simulations (Figure 1G), we found a
243 larger spill-over of DA into the surrounding areas in VS (Figure 2F and Figure S3D, E).
244 Significant amounts of extracellular DA also remained 100 ms after the physiologically
245 relevant 6APs/20Hz firing stimulus. At the receptor level, D1R occupancy in VS showed a
246 similar response to that in DS during the burst (Figure 1I, 2G and Video 2). By contrast, D2R
247 occupancy during pacemaker activity was higher in VS than DS (~0.8 versus ~0.55 in DS), in

248 accordance with the higher prevailing basal DA concentration. Additionally, the larger DA
249 overflow in VS after a burst caused a higher relative increase in receptor occupancy further
250 away from the area actively bursting than compared to DS (Figure 2H). A pause in firing had
251 the same effect on D2R as in DS (Figure S3F).
252

253 ## Changes to uptake capacity greatly affects [DA] in the ventral striatum

254 The values used to model the striatum (Table 1) in the previous simulations were chosen to
255 best mimic the physiological system found in vivo. However, to test the robustness of the
256 results, we performed simulations across wide ranges of the variable key parameters on
257 which the model is based. First, we varied the number of varicosities actively releasing DA
258 by setting the varicosity density to one site per 9 μm^3 *(Doucet et al., 1986)* and simulating 4
259 Hz pacemaker activity with the release-capable fraction ranging from 5% to 100% (reported
260 values range from 20% to virtually all) *(Ducrot et al, 2021; Liu et al., 2021; Liu et al, 2018;*
261 *Pereira et al, 2016)* (Figure 3A). As the fraction of active sites increased, DA concentrations
262 increased at both the median level (50th percentile), which we consider a measure of tonic
263 or baseline DA levels, and at peak levels (99.5^{th} percentile) in both DS and VS (Figure 3B, see
264 Figure S4A for schematic of tonic and peak DA). We then used the $99.5^{th}/50^{th}$ percentile
265 ratio as a measure of the focality of the DA distribution (i.e. hotspot DA relative to baseline
266 DA). This was intended as a measure of heterogeneity, that is, the higher focality, the
267 greater competence for spatially heterogenous signalling, as has been reported in *(Hamid et*
268 *al, 2021; Howe & Dombeck, 2016)*. Quantifying this across the percentage of active
269 terminals showed that the focality of the DA distribution dropped as the active fraction
270 increased in both regions (Figure 3C). However, the percentage of active sites in VS needed

271 to drop to 5% to reach a relative distribution resembling the DS at a full 100% active sites,
272 underscoring a marked difference in the spatial confinement of DA signals in VS and DS.
273 The predicted total DA content of a vesicle and the fraction of content released per
274 fusion event is reported to range from 1,000 to 30,000 molecules *(Garris et al, 1994; Pothos*
275 *et al, 1998; Staal et al, 2004; Sulzer & Pothos, 2000)* (Figure 3D). As expected, tonic and peak
276 concentrations increased in both DS and VS as quantal size was increased (Figure 3E). Also
277 as expected, the focality of the DA distributions dropped for both regions as quantal size
278 increased (Figure 3F). The relative difference in tonic DA, however, remained persistently
279 higher in VS and even increased as quantal size increased, indicating a tendency for VS to
280 maintain basal levels of DA regardless of release content (Figure 3G). The higher end of
281 quantal sizes, however, resulted in median concentrations far beyond what is typically
282 reported (Figure 3E) *(Sulzer et al., 2016)*. We observed largely similar pattern when changing
283 either release probability or firing rate (Figure S4B-G).
284 DAT activity is governed by two parameters: K_m and V_{max} *(Kristensen et al, 2011)*. To
285 mimic competitive inhibition of DAT by e.g., cocaine, we ran a simulation across various K_m
286 values (Figure 3H) showing that increasing K_m caused a linear increase in DA levels,
287 consistent with DAT uptake rate responding almost linearly to increases in [DA] below K_m
288 (Figure 3I). Of note, most microdialysis studies have reported that cocaine increases [DA] to
289 the same degree in both DS and VS; however, these quantifications are usually derived as a
290 ratio of the absolute baseline level *(Carboni et al, 2001; Maisonneuve & Glick, 1992)*. If we
291 divide our simulations of increasing K_m with the basal levels estimated in Figure 3A-C a
292 similar response for DS and VS is found (Figure 5A). Further, we observe a convergence on a
293 two-fold difference in the absolute values at both tonic and peak levels, which matches
294 reports from earlier FSCV studies (Figure S5B) *(Wu et al, 2001)*. This regionally differential

295 response to cocaine matches our observations in a previous biosensor-based study
296 *(Jorgensen et al., 2023)*.
297 Finally, we changed V_{max} by ± 50% in both regions and observed a smaller change in
298 for tonic level in DS (11 nM) than in VS (38 nM) (Figure 3K). This suggests modulation of V_{max}
299 has higher impact in VS than DS. Further, the impact of changing V_{max} in VS was independent
300 of both Q and $R_{\%}$ within values typically reported in the literature (Figure S5C, D). In contrast
301 to the changes in tonic levels, the relative effect V_{max} had on peak levels was much more
302 modest (Figure 3L).
303 Changes to uptake rate may be mediated by DAT internalization pathways but to our
304 knowledge there is not in vivo evidence of differential release-uptake balances between
305 animals that could lead to varying tonic DA levels across animals. We therefore reanalysed
306 data from our previously published comparison of fibre photometry and microdialysis and
307 found evidence of natural variations in the release-uptake balance of the mice (Figure S5F,
308 G), which may underlie different tonic levels of DA in the striatum between animals.
309

310 ## DAT nanoclustering affects steady state [DA] and clearance after bursts

311 Our simulations highlight DAT V_{max} as an effective regulator of extracellular DA levels in VS
312 (Figure 3K). Internalization of DAT can serve as a mechanism for this control but is a
313 relatively slow process operating on the order of minutes *(Kristensen et al., 2011)*.
314 Interestingly, our recent studies have provided evidence that DAT move laterally in the
315 plasma membrane and transition from a clustered to an unclustered nanoscale distribution
316 in response to excitatory drive and other inputs *(Lycas et al, 2022; Rahbek-Clemmensen et*
317 *al, 2017)*. This led us to hypothesize that DAT nanoclustering serve as a mechanism for
318 regulating DAT activity on a faster time scale. We speculated that dense nanoclusters of DAT

319 would produce domains of low [DA] due to uptake overpowering diffusion (Figure 4A). As
320 uptake rate is concentration dependent, this would reduce uptake efficiency (Figure 4B). To
321 address this hypothesis, we simulated a single ellipsoid varicosity of 1.5 μm in length and
322 800 nm thick with surrounding extracellular space *(Ducrot et al., 2021)*. The surface was
323 unfolded to a square of equal area (Figure 4D), and as 9-16.4% of terminals in the striatum
324 are estimated to be dopaminergic *(Hokfelt, 1968; Tennyson et al, 1974)*, we set the volume
325 of the surrounding space to seven times the varicosity volume. On the surface of the
326 varicosity, we randomly distributed eight DAT nanoclusters (Figure 4C) and ran simulations
327 of how DAT clustering density influenced the DA clearance from the surrounding space. The
328 observed DA concentration in the space surrounding the varicosity shown in Figure 4C is
329 illustrated by the cross-section shown in Figure 4D. Mean DA uptake capacity of the entire
330 space was kept constant at 4 $\mu M\ s^{-1}$ (between the values observed for DS and VS)
331 throughout the simulations, representing a constant amount of DAT molecules on the
332 surface of the varicosity. We only changed the fraction of the surface of the varicosity that
333 was uptake competent by altering the cluster size from small clusters of high density to
334 large clusters of lower density. We ran simulations of eight identical clusters at either 20, 40,
335 80 or 160 nm in diameter to mirror experimentally observed cluster sizes on DA varicosities,
336 as well as a scenario with DAT fully dispersed (Figure 4E) *(Lycas et al., 2022; Rahbek-*
337 *Clemmensen et al., 2017)*. We first performed a test to see the effect clustering would have
338 at steady state concentrations during pacemaker activity. In the unclustered scenario,
339 average [DA] in the simulation hovered at ~15 nM (Figure 4F). However, upon changing to a
340 clustered architecture, [DA] rapidly increased up to 100% (~30 nM) in just 400 ms depending
341 on the degree of clustering (Figure 4F). We further wanted to test what effect
342 nanoclustering would have on clearance after burst activity. To do this, we set the

343 extracellular space to a [DA] of 100 nM and performed simulations for the same clustering
344 scenarios (Figure 4G). Cluster size dramatically affected clearance time, with the most dense
345 clusters taking almost 400 ms to reduce [DA] to 5 nM, compared to just ~200 ms for the
346 unclustered scenario. The hyper-local low-[DA] environment that arose around the dense
347 DAT clusters became apparent when we plotted the [DA] at the centre of a cluster
348 compared to the mean [DA] of the extracellular space (Figure 4H – unclustered also showed
349 drop from surface of varicosity to mean of extracellular space; see general gradient of [DA]
350 in Fig 4D). For the 20 nm cluster-scenario, the clearance was almost entirely limited by how
351 quickly DA diffused to the nanocluster, as the local [DA] dropped to near zero. We originally
352 hypothesized the effect would mainly be due to a depression in [DA] at the very cluster
353 centre, but a concentration profile of the 80 nm cluster-scenario revealed the entirety of the
354 cluster was enveloped in a low-[DA] environment (Figure 4I). Accordingly, if DA receptors
355 are located directly next to a dense nanocluster, this effect could feasibly alter the
356 concentration the individual receptors are exposed to.
357 Summarized, the data supports that DAT nanoclusters produce domains of low [DA]
358 as uptake outcompetes diffusion. As transporter uptake is concentration dependent, the
359 overall uptake efficiency is reduced, which in turn may lead to higher extracellular
360 concentrations of DA. The simulations therefore posit DAT nanoclustering as an efficient
361 way to regulate the extracellular levels of both tonic DA and the spatiotemporal [DA]
362 profiles following release.
363

364 ## DAT clusters more in the ventral striatum

365 As our simulations suggest that nanodomain clustering is a way of regulating uptake, and
366 this may be particularly efficient at controlling extracellular DA in VS, we hypothesized

367 nanoscale clustering would be more prominent in VS. To investigate this, we reanalysed
368 data from a previous publication *(Sorensen et al., 2021)*, where we acquired super-
369 resolution images of coronally sliced striatal sections from mice stained for DAT. For the
370 present study, images were split in DS and VS based on where in the slices they were taken
371 (Figure 4J). DA terminals were identified by vesicular monoamine transporter 2 (VMAT2)
372 expression, and qualitatively DAT appeared more clustered in VS than DS (Figure 4K). To
373 quantify this, we applied the clustering algorithm Density-Based Spatial Clustering of
374 Applications with Noise (DBSCAN) (Figure 4L). This confirmed a regional difference with
375 more DAT localized clusters when using DBSCAN to identify clusters with scanning diameter
376 of 80 nm in VS compared to DS (Figure 4L, M), and we observed a similar regional difference
377 across the range of cluster sizes typically reported (20 to 200 nm; Figure 4N) *(Lycas et al.,*
378 *2022; Rahbek-Clemmensen et al., 2017)* supporting the conclusion that DAT nanoclustering
379 is more prevalent in VS than DS.

380 ## Discussion

381 We developed a three-dimensional, finite-difference computational model to investigate
382 spatiotemporal DA dynamics of striatal subregions in detail. Leveraging prior experimental
383 information on regional differences in dopaminergic innervation density and DAT uptake
384 capacity, our model predicts important differences in dopaminergic dynamics between DS
385 and VS. Strikingly, our simulations suggest that large areas of the DS are effectively devoid
386 of a basal level of DA at pacemaker activity, whereas VS maintain a more homogenous
387 tonic-like basal DA concentration with only small changes in uptake activity powerfully
388 regulating the extracellular DA tone. Furthermore, we modelled receptor binding kinetics
389 and found that D1R binding faithfully followed recently described rapid DA dynamics of the
390 striatum *(Ejdrup et al., 2023; Jorgensen et al., 2023; Markowitz et al, 2023)*, while D2R, with
391 an off-rate of ~5 seconds, appeared better suited for detecting background tone and
392 integrating prolonged activity *(Howe et al, 2013; Jorgensen et al., 2023)*. Collectively, these
393 observations have important implications for our understanding of striatal function in
394 behaviour, including decoding of inputs from the prefrontal cortex (PFC) and limbic system
395 as well as the influential phasic-tonic model of dopaminergic signalling *(Grace et al, 2007;*
396 *Niv et al., 2007; Schultz, 2007)*

397 It has been assumed for long that there are tonic levels of DA in the striatum *(Niv et*
398 *al., 2007; Schultz, 2007; Sulzer et al., 2016)*, although the phenomenon has no clear
399 definition *(Berke, 2018)*. Our simulation of DA dynamics in DS during pacemaker-activity
400 showed no evidence for a homogenous extracellular distribution. Rather, elevated [DA] was
401 transiently present around release sites during pacemaker activity with the remaining space
402 mostly depleted of DA. The absence of a general tonic DA level in DS predicted by our model

403 directly supports the notion that DA release sites in DS establish distinct and only partially
404 overlapping DA domains rather than diffuse, tonic DA levels (see *(Liu et al., 2021)*). This
405 conclusion aligns with recent data where we found that DA concentrations measured by
406 microdialysis correlates with the average of rapid activity recorded with fibre photometry
407 rather than a baseline DA tone *(Ejdrup et al., 2023)*. Earlier modelling work by Wickens and
408 colleagues predicted pacemaker activity would generate a tonic, uniform concentration
409 *(Arbuthnott & Wickens, 2007)*. But our modelling suggested this is prevented by the
410 significant DA uptake capacity of the DS, as measured by more recent reuptake studies (see
411 Table S2).

412 In contrast to the DS, our model predicted VS to hold a considerable basal level of DA
413 even in spaces without an immediately adjacent release site. This is conceivably what most
414 refer to as tonic DA. In this study, we quantified tonic DA as the median concentration of the
415 entire space (50th percentile), which appeared significantly higher in VS than DS because of
416 the lower VS uptake capacity. Importantly, this matches the results of our direct in vivo
417 comparison of DS and VS in freely moving mice *(Jorgensen et al., 2023)*, as well as
418 supporting a spatial gradient of time horizons in the striatum previously predicted in a
419 separate work by Wickens and colleagues *(Wickens et al, 2007)* and measured in vivo by
420 Mohebi and colleagues *(Mohebi et al., 2024)*.

421 To challenge our model predictions, we performed our simulations across a wide
422 range of parameters. Only changes to V_{max} for uptake generated differential responses in
423 the two regions. With release and uptake parameters at values from the literature, VS was
424 at a critical point where minor changes to uptake significantly impacted the tonic levels
425 without any major effect on peak concentrations.

426 Contrary to our observations, some previous microdialysis experiments have
427 suggested higher basal DA levels in the DS compared to VS (Kuczenski & Segal, 1992; Shen et
428 al., 2004 have reported 2-4 times higher [DA] in DS compared to VS *(Kuczenski & Segal,*
429 *1992; Shen et al, 2004)*.However, there are disparate observations in the literature (e.g.
430 Carboni et al., 2001 reported 20% higher [DA] in VS *(Carboni et al., 2001)*. Moreover, it is
431 important to note that regional comparisons in microdialysis might be confounded by the
432 considerably higher uptake rate in DS. This will increase the extraction fraction and possibly
433 lead to a significant overestimation of the extracellular concentration as compared to a
434 region with lower uptake rate, such as the VS *(Chefer et al, 2009)*.
435 Our three-dimensional simulations highlight DAT-mediated reuptake as a key
436 mechanism governing striatal DA dynamics and as a key mediator of regional-specific DA
437 dynamics. A physiologically relevant way to regulate uptake capacity is moving DAT to-and-
438 from the plasma membrane. Indeed, DAT is subject to such regulation and some of these
439 mechanisms may even be exclusive to the ventral region, including protein kinase C-induced
440 DAT internalization and Vav2 regulation of DAT surface expression *(Fagan et al, 2020; Zhu et*
441 *al, 2015)*. Chemogenetic G_q-coupled DREADD activation of DA neurons also result in
442 differential DAT trafficking in the two regions *(Fagan et al., 2020; Kearney et al., 2023)*. The
443 findings position DAT regulation as an excellent candidate for changing tonic DA levels in VS,
444 which has been proposed to selectively attenuate afferent drive from the PFC through D2R
445 activation *(Grace et al., 2007)*. Recent studies of D2R expressing spiny projection neurons
446 (SPNs) in the VS also suggest that the receptor is not fully saturated under basal firing *(Lee*
447 *et al, 2020)*, matching both our simulations of receptor binding and the notion that tonic DA
448 can be manipulated to alter D2R activation.

449 If changing uptake capacity is to have a behavioural relevance on a fast timescale, a
450 mechanism to regulate DAT function faster than internalization must exist. Importantly, the
451 transporter does not only move to-and-from the surface, but also laterally in the plasma
452 membrane. We have reported that DAT forms nanoclusters in the plasma membrane that
453 dynamically reshape based on excitatory and inhibitory input *(Lycas et al., 2022; Rahbek-*
454 *Clemmensen et al., 2017)*. Moreover, we have previously shown that cocaine, which both
455 competitively inhibits DAT and reorganizes the transporter nanodomains *(Lycas et al.,*
456 *2022)*, changes the DA signal of the DS to dynamics akin to the VS *(Jorgensen et al., 2023)*.
457 Importantly, our simulations showed that nanoclustering may be an effective way to
458 sequester DAT in a dense domain where uptake overpowers diffusion and as a result brings
459 down effective uptake speed through local DA depletion. This is in line with evidence that
460 these DAT nanoclusters are enriched in phosphatidylinositol-4,5-bisphosphate (PIP2), and
461 that metabolism of PIP2 decreases uptake rate of DAT *(Lycas et al., 2022)*; Carvelli, 2002
462 #2339}. We also found that the nanoclustering phenomenon was considerably more
463 prevalent in VS than in DS. Taken together, these data point to DAT nanoclustering as a way
464 to shape both the spatiotemporal profile of DA release as well as the tonic levels of DA in
465 the striatum – particularly in the VS.
466 Our incorporation of receptor binding was inspired by important previous modelling
467 work *(Dreyer et al., 2010; Dreyer & Hounsgaard, 2013; Hunger et al, 2020)*. However, earlier
468 models by Dreyer & colleagues assumed instantaneous equilibrium between extracellular
469 DA and receptor occupation, which disregards differences in kinetics of the DA receptors
470 that greatly impact transmission dynamics. While later work by Hunger & colleagues
471 introduce more complex receptor modelling, they based their kinetics parameters on early
472 pharmacological studies, whose values likely would prevent DA receptors from decoding

473 signal below the order of minutes *(Burt et al, 1976; Maeno, 1982; Nishikori et al, 1980; Sano*
474 *et al, 1979)*. Instead, we based our receptor kinetics on newer pharmacological experiments
475 in live cells *(Agren et al., 2021)* and properties of the recently developed DA receptor-based
476 biosensors *(Labouesse & Patriarchi, 2021)*, whose receptor values match well despite
477 different methodological approaches. The biosensors are mutated receptors whose kinetics
478 may not be identical to the endogenous receptors, but only the intracellular domains are
479 altered, with no apparent changes of the binding site *(Labouesse & Patriarchi, 2021)*.
480 Indeed, these biosensors exhibit kinetics that are well aligned with both modelled and
481 experimentally reported extracellular DA dynamics using non-biosensor-based methods
482 *(Atcherley et al., 2015; Gonon et al., 2000; Venton et al, 2002)*. We believe accordingly that
483 our updated parameters are more accurate portrayals of *in vivo* conditions; however, as
484 shown throughout the study, the affinity values greatly affect the results. Therefore, we find
485 it important that our model will be available to the research community, allowing others to
486 test their own estimates of receptor kinetics and assess their impact on the model's
487 behaviour.
488 The presented simulations suggested that receptor binding was largely invariant to
489 single release events during pacemaker activity, while bursts of activity rapidly changed
490 occupancy. Both D1R and D2R immediately responded to burst onset; however, while D1R
491 occupancy rapidly declined to zero within approximately 50 ms, the slow D2R kinetics
492 resulted in an occupancy decline over ~5 seconds, returning to the baseline maintained by
493 tonic firing. This means that D1R is better suited to discriminate inputs in rapid succession
494 and allow for postsynaptic decoding of the fast-paced in vivo dynamics described in
495 particularly for DS *(Ejdrup et al., 2023; Jorgensen et al., 2023; Markowitz et al., 2023)*. By
496 contrast, our analysis shows that D2Rs integrate DA signals over several seconds. As D1R

occupancy is negligible during pacemaker activity and D2R kinetics are too slow to pick up rapid changes in DA concentration, our simulations moreover suggest pauses in firing of less than 1 second is not an effective way of signalling for the striatal dopaminergic system. Notably, this finding was apparent even when the D2 affinity was increased an order of magnitude. This challenges the effectiveness of proposed negative reward prediction errors, as even a long pause in firing would have a limited effect on D2 receptor occupation and downstream signaling. This may explain why DA drops during reward omissions are not nearly as prominent as positive signals *(Farrell et al, 2022; Greenstreet et al, 2025)*..

In conclusion, we have developed a three-dimensional model for DA release dynamics and receptor binding that integrates a wealth of experimentally determined parameters and generates responses to electrical and pharmacological input that fits robustly with literature observations. The model offers an important theoretical framework and a predictive tool that can serve as the basis for future experimental endeavours and help guide the interpretation of new as well as older empirical findings on DA signalling dynamics under both physiological conditions and in disease.

512 # Methods

513 ## Three-dimensional finite difference model

514 DA release sites in the striatum were simulated at a density of one site per 25 μm^3 in DS and
515 one site per 27.8 μm^3 in VS (except for Figure 4b and c). As a single medium spiny neuron in
516 the striatum is estimated to be influenced by axons from 95 to 194 dopaminergic neurons
517 *(Matsuda et al, 2009)*, we simulated DA release sites as originating from 150 separate cell
518 bodies. These were set to fire independently from each other at 4 Hz generated by a Poisson
519 distribution. We set the release probability in response to an action potential at the
520 individual terminal levels to 6% *(Dreyer et al., 2010)*, and if a release occurred the DA
521 concentration of the voxel was elevated by the equivalent of 3000 DA molecules as per
522 Equation 1. The volume of each voxel was corrected for an extracellular volume fraction of
523 0.21 *(Rice & Nicholson, 1991)*.

524 We did not incorporate paired-pulse depression in our model as most in vivo FSCV
525 studies have not reported this phenomenon *(Chergui et al, 1994; Garris & Wightman, 1994;*
526 *Hamid et al, 2016; May & Wightman, 1989)*. In addition, we could explain the gradual blunt
527 of the response during prolonged stimulation (Figure 2E) as the result of an equilibrium
528 between release and uptake rather than a depression in release. Newer in vivo biosensor-
529 based studies observe the same "blunting" phenomenon during stimulation trains *(Mohebi*
530 *et al, 2023)*. A low initial release probability that scales well with frequency has also been
531 reported for VMAT2-positive release sites in dopaminergic cultures where the axons are not
532 severed from their cell bodies as in acute striatal slices *(Silm et al, 2019)*. Note that we did
533 not explicitly model autoreceptor inhibition at pacemaker activity. However, this value
534 should be implicitly reflected in the in vivo estimates we base our model on.

When simulating bursts or trains of stimulations, action potentials were added as described for each simulation, but release probability was kept the same unless otherwise noted. Uptake was evenly distributed throughout the simulation space with a V_{max} at 6 µm s^{-1} for DS and 2 µm s^{-1} for VS (see Table S2) and a K_m at 210 nM *(Hovde et al, 2019)* and calculated for each voxel as per Equation 2. For each time step, *dt*, diffusion calculated with a finite difference implementation of the Laplacian operator described in Equation 3 using a diffusion coefficient corrected for tortuosity at 321.7 μm^2 s^{-1}. Periodic boundaries were used to avoid edge issues with a simulation size of 50x50x50 µm unless otherwise noted. The Python-based implementation of the model can be found as described in the Code and Data Availability section.

Receptor occupancy

Our modelling of receptor binding was based on the work of (*Dreyer & Hounsgaard, 2013).* Occupancy of the receptors for any given voxel was calculated numerically by numerical integration of:

(6)

$$\frac{d\mathrm{D}_x\mathrm{R}_{\mathrm{occ,t}}}{d\mathrm{t}} = [\mathrm{DA}]_t\, k_{on}\, (1 - \mathrm{D}_x\mathrm{R}_{occ,t}) - k_{off}\, \mathrm{D}_x\mathrm{R}_{occ,t}$$

Where $[DA]_t$ was the dopamine concentration at the given voxel, $D_xR_{occ,t}$ the fraction of DA recptors occupied in the same voxel, k_{on} the rate constant and k_{off} the reverse rate constant. The model assumed no buffering effect from DA bound to receptors, as DA receptors are GPCRs typically expressed at very low levels *(Zhang et al, 2024)*.

556 ## Immunohistochemistry analysis

557 Analysed widefield images were obtained from *(Sorensen et al., 2021)*. The mouse striatum
558 slices were stained for either DAT or VMAT2 (see Sørensen et al., 2021 for slicing, fixation,
559 staining and imaging protocol *(Sorensen et al., 2021)*. Fluorescence intensities were
560 extracted in a single dorsoventral line parallel to the midline through the horizontally centre
561 of the anterior commissure using ImageJ v1.53q. for each slice. Data was vertically centred
562 around the anterior commissure. No background subtraction was performed.

563

564 ## FSCV modelling

565 FSCV recordings were modelled by convoluting a simulated DA response to a pseudo FSCV
566 trace. The impulse function used was as described in *(Venton et al., 2002)*. In brief, the
567 impulse function was defined as $\mathrm{IF_{FSCV}} = e^{-(t+1)(k_{-1}*t_s+k_{-2}*t_o)}$, where t is time, t_s is scan
568 time, t_o is oxidization time, and k_{-1} and k_{-2} desorption constants. t_s was set to 100 ms as
569 reported in *(May & Wightman, 1989)* and t_o to 4 ms, which is half of the typically reported
570 symmetrical waveform length. The desorption constants (k_{-1} = 1.2 s^{-1} and k_{-2} = 12 s^{-1}) were
571 taken directly from *(Venton et al., 2002)*.

572

573 ## Nanocluster uptake modelling

574 Nanoclustering of DAT was simulated in Python. An ellipsoid-shaped varicosity of 1.5 μm in
575 length and 800 nm in width was modelled as a flat, square surface with a width of 1.8 μm to
576 match the total surface area *(Lycas et al., 2022; Rahbek-Clemmensen et al., 2017)*. As 9-
577 16.4% of terminals in the striatum are estimated to be dopaminergic*(Hokfelt, 1968;*
578 *Tennyson et al., 1974)*, we set the height of the simulation space to 3.52 μm to generate an

579 extracellular volume seven times the size of the varicosity. Axons and cell bodies are likely a
580 non-negligible part of the striatal volume but omitted in this analysis due to a lack of
581 information in the literature (however, decreasing the share of striatal space taken up by DA
582 varicosities works in the direction of our hypothesis). Spatial granularity was set to 20 nm,
583 and we randomly placed eight non-overlapping locations for clusters on the simulated
584 varicosity. Uptake capacity per voxel for each clustering scenario was set so the mean
585 uptake of the entire space was 4 μm s^{-1}, which resulted in clusters with increased DAT
586 density with decreasing cluster size.

587 For the steady state simulations, we added [DA] at a constant rate of 224 nM s^{-1}
588 calculated as follows:

589 (7)

590 $$[DA]_{add} = Q_{conc}\, \mathrm{f_{rate}}\, \mathrm{R_{\%}}\, AT_{density}$$

591 Where $[DA]_{add}$ was the DA concentration added per second, Q_{conc} the DA concentration
592 added to a voxel by a single release event, $\mathrm{f_{rate}}$ the firing rate at pacemaker activity, $\mathrm{R_{\%}}$ the
593 probability of release for each action potential and $AT_{density}$ the density of actively
594 releasing terminals. Q_{conc} was calculated as follows:

595 (8)

596 $$Q_{conc} = \frac{Vesicle_{vol}}{Voxel_{vol}}\, Vesicle_{conc}\, \frac{1}{EVF}$$

597 Where $Vesicle_{vol}$ is the volume of a vesicle (with an assumed radius of 25 nm), $Voxel_{vol}$
598 the volume of a voxel in the simulation space, $Vesicle_{conc}$ the concentration of DA in a
599 single vesicle (assuming 3000 DA molecules) and EVF the extracellular volume fraction of
600 the striatum.

601 For the clearance after burst simulations, we set the initial DA concentration of the
602 entire space to 100 nM.
603 We ran all the nanoclustering simulations with a time step of $1.875e^{-7}$ s to avoid
604 numerical instability. Diffusion corrected for tortuosity was set to 321.7 $\mu m^2 s^{-1}$ and
605 calculated with a Laplacian operation as described in Equation 3. Periodic boundaries were
606 used to account for the varicosity being circular and avoid issues at the edge of the
607 simulation space. The full implementation in Python can be found as described in the Code
608 and Data Availability section.
609

610 ## Super-resolution clustering analysis

611 Super-resolved fluorescence microscopy dual color images from *(Sorensen et al., 2021)* of
612 striatal brain slices from mice were analyzed based on their position in the dorsal or ventral
613 regions (Figure 4J). Localizations were fitted using DAOSTORM *(Babcock et al, 2012)* on the
614 originally acquired direct stochastic optical reconstruction microscopy (dSTORM) videos
615 with the following settings: background sigma of 8, maximum likelihood estimation as the
616 fitting error model, 20 peak identification iterations, an initial sigma estimate of 1.5 and a
617 threshold adjusted to each imaging session. Each image was analysed for percentage of
618 localizations within a cluster using density-based spatial clustering of applications with noise
619 (DBSCAN) *(Ester et al, 1996)* using the Python package Scikit-learn 0.22 *(Pedregosa et al,*
620 *2021)*. To uncover broader trends, we scanned across a range of parameters: radius was run
621 from 10 nm to 200 nm and number of localizations from 10 to 200. For Figure 4M a
622 diameter of 80 nm was chosen to match the size reported in *(Rahbek-Clemmensen et al.,*
623 *2017)*.
624

Statistical Analysis

The statistical analyses performed can be found in the legends of each figure. Statistical analyses were performed using open-source python packages SciPy v1.5.2 and NumPy v1.18.1. Boxplots show the 25th and 75th percentile range and whiskers indicate up to 1.5 times the interquartile range. The remaining data points are plotted as individual outliers.

Acknowledgements

We thank Dr. Kenneth L. Madsen, University of Copenhagen for general input on our modelling and Dr. Nicolas Tritsch, New York University Grossman School of Medicine, for a fruitful discussion on the postsynaptic receptor properties and occupation.

Additional Information

Competing Interest

Authors declare that they have no competing interests.

Funding

The work was supported by the Lundbeck Foundation grants R266-2017-4331 (UG), R276-2018-792 (UG), R359-2020-2301 (UG), R181-2014-3090 (FH) and R303-2018-3540 (FH).

Author Contributions

ALE, FH and UG conceptualized the study. ALE built the model with help from JKD. ALE ran the simulations. MDL and SHJ provided technical input on experimental data. ALE drafted the manuscript. ALE, FH and UG wrote the final version of the manuscript with comments

and suggestions from JKD, TWR and JWD. All authors critically evaluated the manuscript. FH and UG supervised the project.

Additional files

Supplementary file

Supplementary Text.

Figures S1 to S5.

Tables S1 and S2.

Videos 1 and 2.

Data Availability

Numerical implementation and code to run the simulations are available at: https://github.com/GetherLab/striatal-dopamine-modelling. All experimental data are from *(Ejdrup et al., 2023)* or *(Sorensen et al., 2021)*. Corresponding authors on these papers should be consulted for data availability.

665 ## References

666 Agnati LF, Bjelke B, Fuxe K. 1995. Volume versus wiring transmission in the brain: a new
667 theoretical frame for neuropsychopharmacology. *Med Res Rev* **15**: 33-45.
668 10.1002/med.2610150104

669 Agren R, Stepniewski TM, Zeberg H, Selent J, Sahlholm K. 2021. Dopamine D(2) Receptor
670 Agonist Binding Kinetics-Role of a Conserved Serine Residue. *Int J Mol Sci*
671 **22**10.3390/ijms22084078

672 Arbuthnott GW, Wickens J. 2007. Space, time and dopamine. *Trends Neurosci* **30**: 62-69.
673 10.1016/j.tins.2006.12.003

674 Atcherley CW, Laude ND, Monroe EB, Wood KM, Hashemi P, Heien ML. 2015. Improved
675 Calibration of Voltammetric Sensors for Studying Pharmacological Effects on Dopamine
676 Transporter Kinetics in Vivo. *ACS Chem Neurosci* **6**: 1509-1516. 10.1021/cn500020s

677 Babcock H, Sigal YM, Zhuang X. 2012. A high-density 3D localization algorithm for stochastic
678 optical reconstruction microscopy. *Opt Nanoscopy* **1**10.1186/2192-2853-1-6

679 Berke JD. 2018. What does dopamine mean? *Nat Neurosci* **21**: 787-793. 10.1038/s41593-018-
680 0152-y

681 Beyene AG, McFarlane IR, Pinals RL, Landry MP. 2017. Stochastic Simulation of Dopamine
682 Neuromodulation for Implementation of Fluorescent Neurochemical Probes in the Striatal
683 Extracellular Space. *ACS Chem Neurosci* **8**: 2275-2289. 10.1021/acschemneuro.7b00193

684 Block ER, Nuttle J, Balcita-Pedicino JJ, Caltagarone J, Watkins SC, Sesack SR, Sorkin A. 2015.
685 Brain Region-Specific Trafficking of the Dopamine Transporter. *J Neurosci* **35**: 12845-12858.
686 10.1523/JNEUROSCI.1391-15.2015

687 Borroto-Escuela DO, Perez De La Mora M, Manger P, Narvaez M, Beggiato S, Crespo-Ramirez
688 M, Navarro G, Wydra K, Diaz-Cabiale Z, Rivera A *et al*. 2018. Brain Dopamine Transmission in
689 Health and Parkinson's Disease: Modulation of Synaptic Transmission and Plasticity Through
690 Volume Transmission and Dopamine Heteroreceptors. *Front Synaptic Neurosci* **10**: 20.
691 10.3389/fnsyn.2018.00020

692 Brimblecombe KR, Vietti-Michelina S, Platt NJ, Kastli R, Hnieno A, Gracie CJ, Cragg SJ. 2019.
693 Calbindin-D28K Limits Dopamine Release in Ventral but Not Dorsal Striatum by Regulating
694 Ca(2+) Availability and Dopamine Transporter Function. *ACS Chem Neurosci* **10**: 3419-3426.
695 10.1021/acschemneuro.9b00325

696 Brown HD, McCutcheon JE, Cone JJ, Ragozzino ME, Roitman MF. 2011. Primary food reward
697 and reward-predictive stimuli evoke different patterns of phasic dopamine signaling
698 throughout the striatum. *Eur J Neurosci* **34**: 1997-2006. 10.1111/j.1460-9568.2011.07914.x

699 Burt DR, Creese I, Snyder SH. 1976. Properties of [3H]haloperidol and [3H]dopamine binding
700 associated with dopamine receptors in calf brain membranes. *Mol Pharmacol* **12**: 800-812.

701 Carboni E, Spielewoy C, Vacca C, Nosten-Bertrand M, Giros B, Di Chiara G. 2001. Cocaine and
702 amphetamine increase extracellular dopamine in the nucleus accumbens of mice lacking the
703 dopamine transporter gene. *J Neurosci* **21**: RC141: 141-144. 20015177 [pii]

704 Cardozo DL, Bean BP. 1995. Voltage-dependent calcium channels in rat midbrain dopamine
705 neurons: modulation by dopamine and GABAB receptors. *J Neurophysiol* **74**: 1137-1148.
706 10.1152/jn.1995.74.3.1137

707 Chefer VI, Thompson AC, Zapata A, Shippenberg TS. 2009. Overview of brain microdialysis.
708 *Curr Protoc Neurosci* **Chapter 7**: Unit7 1. 10.1002/0471142301.ns0701s47

709 Chergui K, Suaud-Chagny MF, Gonon F. 1994. Nonlinear relationship between impulse flow,
710 dopamine release and dopamine elimination in the rat brain in vivo. *Neuroscience* **62**: 641-
711 645. 10.1016/0306-4522(94)90465-0

712 Cragg SJ, Rice ME. 2004. DAncing past the DAT at a DA synapse. *Trends Neurosci* **27**: 270-277.
713 10.1016/j.tins.2004.03.011

714 Dodson PD, Dreyer JK, Jennings KA, Syed EC, Wade-Martins R, Cragg SJ, Bolam JP, Magill PJ.
715 2016. Representation of spontaneous movement by dopaminergic neurons is cell-type
716 selective and disrupted in parkinsonism. *Proc Natl Acad Sci U S A* **113**: E2180-2188.
717 10.1073/pnas.1515941113

718 Doucet G, Descarries L, Garcia S. 1986. Quantification of the dopamine innervation in adult
719 rat neostriatum. *Neuroscience* **19**: 427-445. 10.1016/0306-4522(86)90272-1

720 Dreyer JK, Herrik KF, Berg RW, Hounsgaard JD. 2010. Influence of Phasic and Tonic Dopamine
721 Release on Receptor Activation. *Journal of Neuroscience* **30**: 14273-14283. Doi
722 10.1523/Jneurosci.1894-10.2010

723 Dreyer JK, Hounsgaard J. 2013. Mathematical model of dopamine autoreceptors and uptake
724 inhibitors and their influence on tonic and phasic dopamine signaling. *J Neurophysiol* **109**:
725 171-182. 10.1152/jn.00502.2012

726 Dreyer JK, Vander Weele CM, Lovic V, Aragona BJ. 2016. Functionally Distinct Dopamine
727 Signals in Nucleus Accumbens Core and Shell in the Freely Moving Rat. *J Neurosci* **36**: 98-112.
728 10.1523/JNEUROSCI.2326-15.2016

729 Ducrot C, Bourque MJ, Delmas CVL, Racine AS, Guadarrama Bello D, Delignat-Lavaud B,
730 Domenic Lycas M, Fallon A, Michaud-Tardif C, Burke Nanni S *et al*. 2021. Dopaminergic
731 neurons establish a distinctive axonal arbor with a majority of non-synaptic terminals. *FASEB*
732 *J* **35**: e21791. 10.1096/fj.202100201RR

733 Ejdrup AL, Wellbourne-Wood J, Dreyer JK, Guldhammer N, Lycas MD, Gether U, Hall BJ,
734 Sorensen G. 2023. Within-Mice Comparison of Microdialysis and Fiber Photometry-Recorded
735 Dopamine Biosensor during Amphetamine Response. *ACS Chem Neurosci* **14**: 1622-1630.
736 10.1021/acschemneuro.2c00817

737 Eriksen J, Jorgensen TN, Gether U. 2010. Regulation of dopamine transporter function by
738 protein-protein interactions: new discoveries and methodological challenges. *J Neurochem*
739 **113**: 27-41. 10.1111/j.1471-4159.2010.06599.x

740 Eriksen J, Rasmussen SG, Rasmussen TN, Vaegter CB, Cha JH, Zou MF, Newman AH, Gether U.
741 2009. Visualization of dopamine transporter trafficking in live neurons by use of fluorescent
742 cocaine analogs. *J Neurosci* **29**: 6794-6808. 29/21/6794 [pii]
743 10.1523/JNEUROSCI.4177-08.2009

744 Ester M, Kriegel H-P, Sander J, Xu X (1996) A density-based algorithm for discovering clusters
745 in large spatial databases with noise. In: *Proc 2nd International Conference on Knowledge*
746 *Discovery and Data Mining*, pp. 226–231. AAAI Press:

747 Fagan RR, Kearney PJ, Sweeney CG, Luethi D, Schoot Uiterkamp FE, Schicker K, Alejandro BS,
748 O'Connor LC, Sitte HH, Melikian HE. 2020. Dopamine transporter trafficking and Rit2 GTPase:
749 Mechanism of action and in vivo impact. *J Biol Chem* **295**: 5229-5244.
750 10.1074/jbc.RA120.012628

751 Farrell K, Lak A, Saleem AB. 2022. Midbrain dopamine neurons signal phasic and ramping
752 reward prediction error during goal-directed navigation. *Cell Rep* **41**: 111470.
753 10.1016/j.celrep.2022.111470

754 Garris PA, Ciolkowski EL, Pastore P, Wightman RM. 1994. Efflux of dopamine from the synaptic
755 cleft in the nucleus accumbens of the rat brain. *J Neurosci* **14**: 6084-6093.
756 10.1523/JNEUROSCI.14-10-06084.1994

757 Garris PA, Wightman RM. 1994. Different kinetics govern dopaminergic transmission in the
758 amygdala, prefrontal cortex, and striatum: an in vivo voltammetric study. *J Neurosci* **14**: 442-
759 450. 10.1523/JNEUROSCI.14-01-00442.1994

760 Gonon F, Burie JB, Jaber M, Benoit-Marand M, Dumartin B, Bloch B. 2000. Geometry and
761 kinetics of dopaminergic transmission in the rat striatum and in mice lacking the dopamine
762 transporter. *Prog Brain Res* **125**: 291-302. 10.1016/S0079-6123(00)25018-8

763 Grace AA, Floresco SB, Goto Y, Lodge DJ. 2007. Regulation of firing of dopaminergic neurons
764 and control of goal-directed behaviors. *Trends Neurosci* **30**: 220-227.
765 10.1016/j.tins.2007.03.003

766 Greenstreet F, Vergara HM, Johansson Y, Pati S, Schwarz L, Lenzi SC, Geerts JP, Wisdom M,
767 Gubanova A, Rollik LB *et al*. 2025. Dopaminergic action prediction errors serve as a value-free
768 teaching signal. *Nature*10.1038/s41586-025-09008-9

769 Hamid AA, Frank MJ, Moore CI. 2021. Wave-like dopamine dynamics as a mechanism for
770 spatiotemporal credit assignment. *Cell* **184**: 2733-2749 e2716. 10.1016/j.cell.2021.03.046

771 Hamid AA, Pettibone JR, Mabrouk OS, Hetrick VL, Schmidt R, Vander Weele CM, Kennedy RT,
772 Aragona BJ, Berke JD. 2016. Mesolimbic dopamine signals the value of work. *Nat Neurosci* **19**:
773 117-126. 10.1038/nn.4173

774 Hokfelt T. 1968. In vitro studies on central and peripheral monoamine neurons at the
775 ultrastructural level. *Z Zellforsch Mikrosk Anat* **91**: 1-74. 10.1007/BF00336984

776 Hovde MJ, Larson GH, Vaughan RA, Foster JD. 2019. Model systems for analysis of dopamine
777 transporter function and regulation. *Neurochem Int* **123**: 13-21.
778 10.1016/j.neuint.2018.08.015

779 Howe MW, Dombeck DA. 2016. Rapid signalling in distinct dopaminergic axons during
780 locomotion and reward. *Nature* **535**: 505-510. 10.1038/nature18942

781 Howe MW, Tierney PL, Sandberg SG, Phillips PE, Graybiel AM. 2013. Prolonged dopamine
782 signalling in striatum signals proximity and value of distant rewards. *Nature* **500**: 575-579.
783 10.1038/nature12475

784 Hunger L, Kumar A, Schmidt R. 2020. Abundance Compensates Kinetics: Similar Effect of
785 Dopamine Signals on D1 and D2 Receptor Populations. *J Neurosci* **40**: 2868-2881.
786 10.1523/JNEUROSCI.1951-19.2019

787 Jones SR, Gainetdinov RR, Jaber M, Giros B, Wightman RM, Caron MG. 1998. Profound
788 neuronal plasticity in response to inactivation of the dopamine transporter. *Proc Natl Acad*
789 *Sci U S A* **95**: 4029-4034.

790 Jorgensen SH, Ejdrup AL, Lycas MD, Posselt LP, Madsen KL, Tian L, Dreyer JK, Herborg F,
791 Sorensen AT, Gether U. 2023. Behavioral encoding across timescales by region-specific
792 dopamine dynamics. *Proc Natl Acad Sci U S A* **120**: e2215230120. 10.1073/pnas.2215230120

793 Kearney PJ, Bolden NC, Kahuno E, Conklin TL, Martin GE, Lubec G, Melikian HE. 2023.
794 Presynaptic Gq-coupled receptors drive biphasic dopamine transporter trafficking that
795 modulates dopamine clearance and motor function. *J Biol Chem* **299**: 102900.
796 10.1016/j.jbc.2023.102900

797 Klaus A, Alves da Silva J, Costa RM. 2019. What, If, and When to Move: Basal Ganglia Circuits
798 and Self-Paced Action Initiation. *Annu Rev Neurosci* **42**: 459-483. 10.1146/annurev-neuro-
799 072116-031033

800 Kristensen AS, Andersen J, Jorgensen TN, Sorensen L, Eriksen J, Loland CJ, Stromgaard K,
801 Gether U. 2011. SLC6 neurotransmitter transporters: structure, function, and regulation.
802 *Pharmacol Rev* **63**: 585-640. 10.1124/pr.108.000869

803 Kuczenski R, Segal DS. 1992. Differential effects of amphetamine and dopamine uptake
804 blockers (cocaine, nomifensine) on caudate and accumbens dialysate dopamine and 3-
805 methoxytyramine. *J Pharmacol Exp Ther* **262**: 1085-1094.

806 Labouesse MA, Patriarchi T. 2021. A versatile GPCR toolkit to track in vivo neuromodulation:
807 not a one-size-fits-all sensor. *Neuropsychopharmacology* **46**: 2043-2047. 10.1038/s41386-
808 021-00982-y

809 Lee SJ, Lodder B, Chen Y, Patriarchi T, Tian L, Sabatini BL. 2020. Cell-type-specific
810 asynchronous modulation of PKA by dopamine in learning. *Nature*10.1038/s41586-020-
811 03050-5

812 Liu C, Cai X, Ritzau-Jost A, Kramer PF, Li Y, Khaliq ZM, Hallermann S, Kaeser PS. 2022. An action
813 potential initiation mechanism in distal axons for the control of dopamine release. *Science*
814 **375**: 1378-1385. 10.1126/science.abn0532

815 Liu C, Goel P, Kaeser PS. 2021. Spatial and temporal scales of dopamine transmission. *Nat Rev*
816 *Neurosci* **22**: 345-358. 10.1038/s41583-021-00455-7

817 Liu C, Kershberg L, Wang J, Schneeberger S, Kaeser PS. 2018. Dopamine Secretion Is Mediated
818 by Sparse Active Zone-like Release Sites. *Cell* **172**: 706-718 e715. 10.1016/j.cell.2018.01.008

819 Lycas MD, Ejdrup AL, Sorensen AT, Haahr NO, Jorgensen SH, Guthrie DA, Stoier JF, Werner C,
820 Newman AH, Sauer M *et al*. 2022. Nanoscopic dopamine transporter distribution and
821 conformation are inversely regulated by excitatory drive and D2 autoreceptor activity. *Cell*
822 *Rep* **40**: 111431. 10.1016/j.celrep.2022.111431

823 Maeno H. 1982. Dopamine receptors in canine caudate nucleus. *Mol Cell Biochem* **43**: 65-80.
824 10.1007/BF00423094

825 Maisonneuve IM, Glick SD. 1992. Interactions between ibogaine and cocaine in rats: in vivo
826 microdialysis and motor behavior. *Eur J Pharmacol* **212**: 263-266. 10.1016/0014-
827 2999(92)90340-a

828 Markowitz JE, Gillis WF, Jay M, Wood J, Harris RW, Cieszkowski R, Scott R, Brann D, Koveal D,
829 Kula T *et al*. 2023. Spontaneous behaviour is structured by reinforcement without explicit
830 reward. *Nature* **614**: 108-117. 10.1038/s41586-022-05611-2

831 Matityahu L, Gilin N, Sarpong GA, Atamna Y, Tiroshi L, Tritsch NX, Wickens JR, Goldberg JA.
832 2023. Acetylcholine waves and dopamine release in the striatum. *Nat Commun* **14**: 6852.
833 10.1038/s41467-023-42311-5

834 Matsuda W, Furuta T, Nakamura KC, Hioki H, Fujiyama F, Arai R, Kaneko T. 2009. Single
835 nigrostriatal dopaminergic neurons form widely spread and highly dense axonal arborizations
836 in the neostriatum. *J Neurosci* **29**: 444-453. 10.1523/JNEUROSCI.4029-08.2009

837 May LJ, Wightman RM. 1989. Effects of D-2 antagonists on frequency-dependent stimulated
838 dopamine overflow in nucleus accumbens and caudate-putamen. *J Neurochem* **53**: 898-906.
839 10.1111/j.1471-4159.1989.tb11789.x

840 Mohebi A, Collins VL, Berke JD. 2023. Accumbens cholinergic interneurons dynamically
841 promote dopamine release and enable motivation. *Elife* **12**10.7554/eLife.85011

842 Mohebi A, Wei W, Pelattini L, Kim K, Berke JD. 2024. Dopamine transients follow a striatal
843 gradient of reward time horizons. *Nat Neurosci* **27**: 737-746. 10.1038/s41593-023-01566-3

844 Nicholson C. 1985. Diffusion from an injected volume of a substance in brain tissue with
845 arbitrary volume fraction and tortuosity. *Brain Res* **333**: 325-329. 10.1016/0006-
846 8993(85)91586-0

847 Nicholson C. 1995. Interaction between diffusion and Michaelis-Menten uptake of dopamine
848 after iontophoresis in striatum. *Biophys J* **68**: 1699-1715. 10.1016/S0006-3495(95)80348-6

849 Nicholson C, Phillips JM. 1981. Ion diffusion modified by tortuosity and volume fraction in the
850 extracellular microenvironment of the rat cerebellum. *J Physiol* **321**: 225-257.
851 10.1113/jphysiol.1981.sp013981

852 Nishikori K, Noshiro O, Sano K, Maeno H. 1980. Characterization, solubilization, and
853 separation of two distinct dopamine receptors in canine caudate nucleus. *J Biol Chem* **255**:
854 10909-10915.

855 Niv Y, Daw ND, Joel D, Dayan P. 2007. Tonic dopamine: opportunity costs and the control of
856 response vigor. *Psychopharmacology (Berl)* **191**: 507-520. 10.1007/s00213-006-0502-4

857 Olson L, Seiger A, Fuxe K. 1972. Heterogeneity of striatal and limbic dopamine innervation:
858 highly fluorescent islands in developing and adult rats. *Brain Res* **44**: 283-288. 10.1016/0006-
859 8993(72)90385-x

860 Paladini CA, Robinson S, Morikawa H, Williams JT, Palmiter RD. 2003. Dopamine controls the
861 firing pattern of dopamine neurons via a network feedback mechanism. *Proc Natl Acad Sci U*
862 *S A* **100**: 2866-2871. 10.1073/pnas.0138018100

863 Pedregosa F, Varoquaux G, Gramfort A, Michel V, Thirion B, Grisel o, Blondel M, Prettenhofer
864 P, Weiss R, Dubourg V *et al*. 2021. Scikit-learn: Machine Learning in Python. *Journal of*
865 *Machine Learning Research* **12**: 2825–2830

866 Pereira DB, Schmitz Y, Meszaros J, Merchant P, Hu G, Li S, Henke A, Lizardi-Ortiz JE, Karpowicz
867 RJ, Jr., Morgenstern TJ *et al*. 2016. Fluorescent false neurotransmitter reveals functionally
868 silent dopamine vesicle clusters in the striatum. *Nat Neurosci* **19**: 578-586. 10.1038/nn.4252

869 Pothos EN, Davila V, Sulzer D. 1998. Presynaptic recording of quanta from midbrain dopamine
870 neurons and modulation of the quantal size. *J Neurosci* **18**: 4106-4118.
871 10.1523/JNEUROSCI.18-11-04106.1998

872 Rahbek-Clemmensen T, Lycas MD, Erlendsson S, Eriksen J, Apuschkin M, Vilhardt F, Jorgensen
873 TN, Hansen FH, Gether U. 2017. Super-resolution microscopy reveals functional organization
874 of dopamine transporters into cholesterol and neuronal activity-dependent nanodomains.
875 *Nat Commun* **8**: 740. 10.1038/s41467-017-00790-3

876 Rice ME, Nicholson C. 1991. Diffusion characteristics and extracellular volume fraction during
877 normoxia and hypoxia in slices of rat neostriatum. *J Neurophysiol* **65**: 264-272.
878 10.1152/jn.1991.65.2.264

879 Richards TL, Zahniser NR. 2009. Rapid substrate-induced down-regulation in function and
880 surface localization of dopamine transporters: rat dorsal striatum versus nucleus accumbens.
881 *J Neurochem* **108**: 1575-1584. 10.1111/j.1471-4159.2009.05910.x

882 Salinas AG, Lee JO, Augustin SM, Zhang S, Patriarchi T, Tian L, Morales M, Mateo Y, Lovinger
883 DM. 2023. Distinct sub-second dopamine signaling in dorsolateral striatum measured by a
884 genetically-encoded fluorescent sensor. *Nat Commun* **14**: 5915. 10.1038/s41467-023-41581-
885 3

886 Sano K, Noshiro O, Katsuda K, Nishikori K, Maeno H. 1979. Dopamine receptors and
887 dopamine-sensitive adenylate cyclase in canine caudate nucleus. Characterization and
888 solubilization. *Biochem Pharmacol* **28**: 3617-3627. 10.1016/0006-2952(79)90408-8

889 Schultz W. 2007. Multiple dopamine functions at different time courses. *Annu Rev Neurosci*
890 **30**: 259-288. 10.1146/annurev.neuro.28.061604.135722

891 Shen HW, Hagino Y, Kobayashi H, Shinohara-Tanaka K, Ikeda K, Yamamoto H, Yamamoto T,
892 Lesch KP, Murphy DL, Hall FS *et al*. 2004. Regional differences in extracellular dopamine and
893 serotonin assessed by in vivo microdialysis in mice lacking dopamine and/or serotonin
894 transporters. *Neuropsychopharmacology* **29**: 1790-1799. 10.1038/sj.npp.1300476

895 Silm K, Yang J, Marcott PF, Asensio CS, Eriksen J, Guthrie DA, Newman AH, Ford CP, Edwards
896 RH. 2019. Synaptic Vesicle Recycling Pathway Determines Neurotransmitter Content and
897 Release Properties. *Neuron* **102**: 786-800 e785. 10.1016/j.neuron.2019.03.031

898 Sippy T, Tritsch NX. 2023. Unraveling the dynamics of dopamine release and its actions on
899 target cells. *Trends Neurosci* **46**: 228-239. 10.1016/j.tins.2022.12.005

900 Sorensen G, Rickhag M, Leo D, Lycas MD, Ridderstrom PH, Weikop P, Lilja JH, Rifes P, Herborg
901 F, Woldbye D *et al*. 2021. Disruption of the PDZ domain-binding motif of the dopamine
902 transporter uniquely alters nanoscale distribution, dopamine homeostasis, and reward
903 motivation. *J Biol Chem* **297**: 101361. 10.1016/j.jbc.2021.101361

904 Stuber GD, Hnasko TS, Britt JP, Edwards RH, Bonci A. 2010. Dopaminergic terminals in the
905 nucleus accumbens but not the dorsal striatum corelease glutamate. *J Neurosci* **30**: 8229-
906 8233. 10.1523/JNEUROSCI.1754-10.2010

907 Staal RG, Mosharov EV, Sulzer D. 2004. Dopamine neurons release transmitter via a flickering
908 fusion pore. *Nat Neurosci* **7**: 341-346. 10.1038/nn1205

909 Sulzer D, Cragg SJ, Rice ME. 2016. Striatal dopamine neurotransmission: regulation of release
910 and uptake. *Basal Ganglia* **6**: 123-148. 10.1016/j.baga.2016.02.001

911 Sulzer D, Pothos EN. 2000. Regulation of quantal size by presynaptic mechanisms. *Rev*
912 *Neurosci* **11**: 159-212. 10.1515/revneuro.2000.11.2-3.159

913 Tennyson VM, Heikkila R, Mytilineou C, Cote L, Cohen G. 1974. 5-Hydroxydopamine 'tagged'
914 neuronal boutons in rabbit neostriatum: interrelationship between vesicles and axonal
915 membrane. *Brain Res* **82**: 341-348. 10.1016/0006-8993(74)90617-9

916 Threlfell S, Clements MA, Khodai T, Pienaar IS, Exley R, Wess J, Cragg SJ. 2010. Striatal
917 muscarinic receptors promote activity dependence of dopamine transmission via distinct
918 receptor subtypes on cholinergic interneurons in ventral versus dorsal striatum. *J Neurosci*
919 **30**: 3398-3408. 10.1523/JNEUROSCI.5620-09.2010

920 Venton BJ, Troyer KP, Wightman RM. 2002. Response times of carbon fiber microelectrodes
921 to dynamic changes in catecholamine concentration. *Anal Chem* **74**: 539-546.
922 10.1021/ac010819a

923 Venton BJ, Zhang H, Garris PA, Phillips PE, Sulzer D, Wightman RM. 2003. Real-time decoding
924 of dopamine concentration changes in the caudate-putamen during tonic and phasic firing. *J*
925 *Neurochem* **87**: 1284-1295. 10.1046/j.1471-4159.2003.02109.x

926 Wickens JR, Budd CS, Hyland BI, Arbuthnott GW. 2007. Striatal contributions to reward and
927 decision making: making sense of regional variations in a reiterated processing matrix. *Ann N*
928 *Y Acad Sci* **1104**: 192-212. 10.1196/annals.1390.016

929 Wiencke K, Horstmann A, Mathar D, Villringer A, Neumann J. 2020. Dopamine release,
930 diffusion and uptake: A computational model for synaptic and volume transmission. *PLoS*
931 *Comput Biol* **16**: e1008410. 10.1371/journal.pcbi.1008410

932 Wu Q, Reith ME, Kuhar MJ, Carroll FI, Garris PA. 2001. Preferential increases in nucleus
933 accumbens dopamine after systemic cocaine administration are caused by unique
934 characteristics of dopamine neurotransmission. *J Neurosci* **21**: 6338-6347.
935 10.1523/JNEUROSCI.21-16-06338.2001

936 Xie K, Wang N, Lin X, Wang Z, Zhao X, Fang P, Yue H, Kim J, Luo J, Cui S *et al*. 2020. Organic
937 electrochemical transistor arrays for real-time mapping of evoked neurotransmitter release
938 in vivo. *Elife* **9**10.7554/eLife.50345

939 Zhang M, Chen T, Lu X, Lan X, Chen Z, Lu S. 2024. G protein-coupled receptors (GPCRs):
940 advances in structures, mechanisms, and drug discovery. *Signal Transduct Target Ther* **9**: 88.
941 10.1038/s41392-024-01803-6

942 Zhu S, Zhao C, Wu Y, Yang Q, Shao A, Wang T, Wu J, Yin Y, Li Y, Hou J *et al*. 2015. Identification
943 of a Vav2-dependent mechanism for GDNF/Ret control of mesolimbic DAT trafficking. *Nat*
944 *Neurosci* **18**: 1084-1093. 10.1038/nn.4060
945
946

947 **Table 1.** List of variables used in simulation of the dorsal striatum.

948

Variable	Abbreviation	Value	Reference
Firing rate		4 Hz	*(Paladini et al, 2003)*
Release probability		6%	*(Dreyer et al., 2010)*
DA molecules per vesicle		3000	*(Klaus et al., 2019)*
Diffusion coefficient		763 $\mu m^2 s^{-1}$	*(Nicholson, 1995)*
Tortuosity		1.54	*(Rice & Nicholson, 1991)*
Vmax		6.0 $\mu m\ s^{-1}$	See Table S2
Km		210 nM	*(Hovde et al., 2019)*
Active terminal density	-	0.04 μm^{-3}	*(Liu et al., 2021)*
Extracellular volume fraction		0.21	*(Rice & Nicholson, 1991)*
Number of neurons in simulation space	-	150	*(Matsuda et al., 2009)*

949

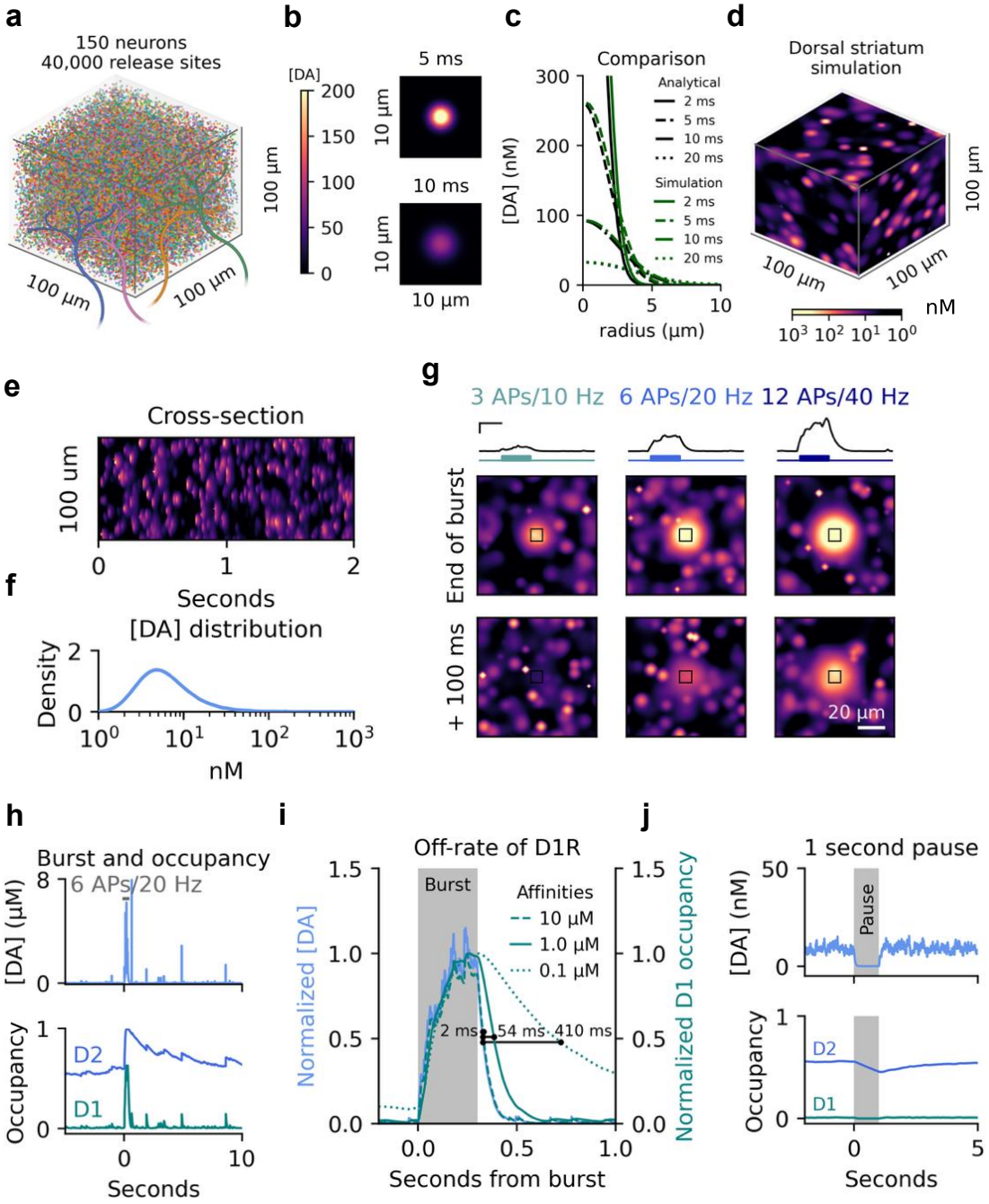

Figure 1. Large-scale 3D model of the dorsal striatum. (**a**) Self-enveloped simulation space of 100^3 µm^3 with approximately 40.000 release sites from 150 neurons. Colours of individual release sites are not matched to neurons. (**b**) Simulation of a single release event after 5 ms and 10 ms. Colour-coded by DA concentration. (**c**) Comparison of analytical solution and simulation of diffusion after a single release event at three different time points. **(d)** Representative snapshot of steady state DA dynamics at 4 Hz tonic firing with parameters mirroring the dorsal striatum. (**e**) Cross-section of temporal dynamics for a midway section through the simulation space shown in (d). (**f**) Histogram of DA concentrations ([DA]) across the entire space in (d). (**g**) DA release during three burst activity scenarios for all release sites in a 10x10x10 µm cube (black boxes) and spill-over into the surrounding space. Burst simulated as increase in firing rate on top of continued tonic firing of the surrounding space.

Traces on top are average DA concentrations for the marked cubes, with bursts schematized by coloured lines below. First image row is at the end of the burst, second row another 100 ms after. Scale bars for traces are 200 ms and 500 nM. Scale bar for the images is 20 µm. (**h**) Top: representative [DA] trace for a voxel with a release site during pacemaker and burst activity. Bottom: Occupancy of D1Rs and D2Rs for same site. **(i)** Zoom on a DA burst as in (h), with [DA] in blue and D1R occupancy in teal with line style indicating different affinities. Shaded area indicates period of bursting with 6 APs at 20 Hz. (**j**) Effect of complete pause in firing for 1 second on both average [DA] and D1R and D2R occupation.

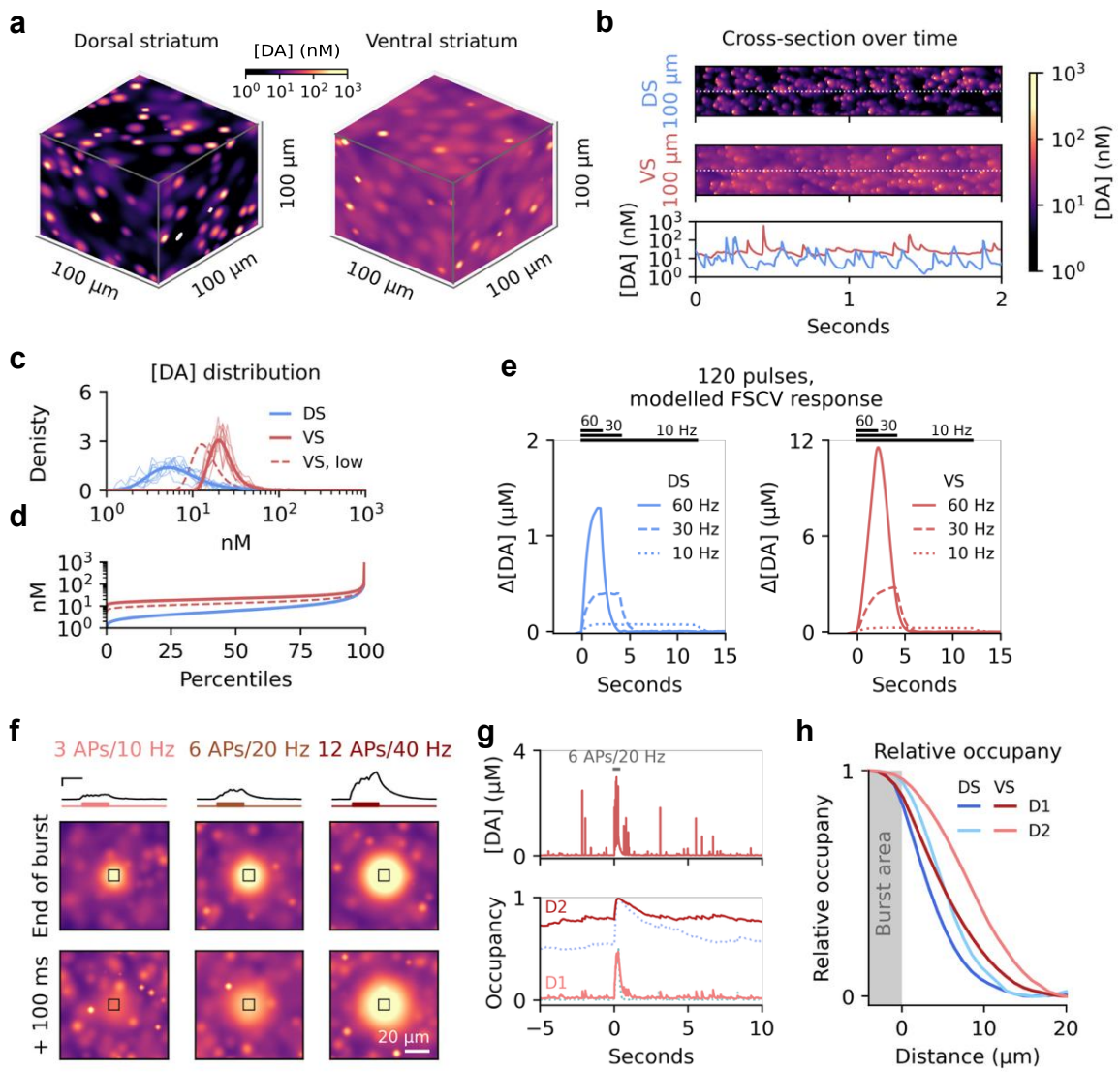

Figure 2. Regional difference in uptake greatly impact DA dynamics. (**a**) Representative snapshots of steady state dynamics at 4 Hz tonic firing with parameters mirroring the dorsal (left) and ventral striatum (right). (**b**) Cross-section of temporal dynamics for data shown in a. Bottom row show concentrations of the dashed lines in the top panels. (**c**) Normalized density of DA concentration of simulations in (a). Thick lines are for the entire space, thin lines are across time for five randomly sampled locations. Dashed red line is for simulation of the ventral striatum with lowest reported innervation density in the literature. (**d**) Same data as in (c), but for concentration percentiles. Note that even the lowest percentiles of VS were above 10 nM in [DA]. (**e**) Convoluted model response (Figure S1c) to mimic FSCV measurements mirroring the experimentally tested stimulation paradigm in *(May & Wightman, 1989)* for the dorsal (left) and ventral striatum (right) (**f**) DA release during three burst activity scenarios for all release sites in a 10x10x10 µm cube (black boxes) and spill-over into the surrounding space. Burst simulated as increase in firing rate on top of continued tonic firing of the surrounding space. Traces on top are average DA concentrations for the marked cubes, with bursts schematized by coloured lines below. First image row is at the end of the burst, second row another 100 ms after. Scale bars for traces are 200 ms and 500 nM. Scale bar for the images is 20 µm. (**g**) Top: representative [DA]

990 trace 1 µm away from a release site during pacemaker and burst activity. Bottom:
991 Occupancy of D1Rs and D2Rs for same site. Occupancy data from corresponding DS
992 simulation on Figure 1k shown in as dotted line. (**h**) Peak occupancy at different distances
993 from the area bursting normalized to maximal and minimum occupancy.

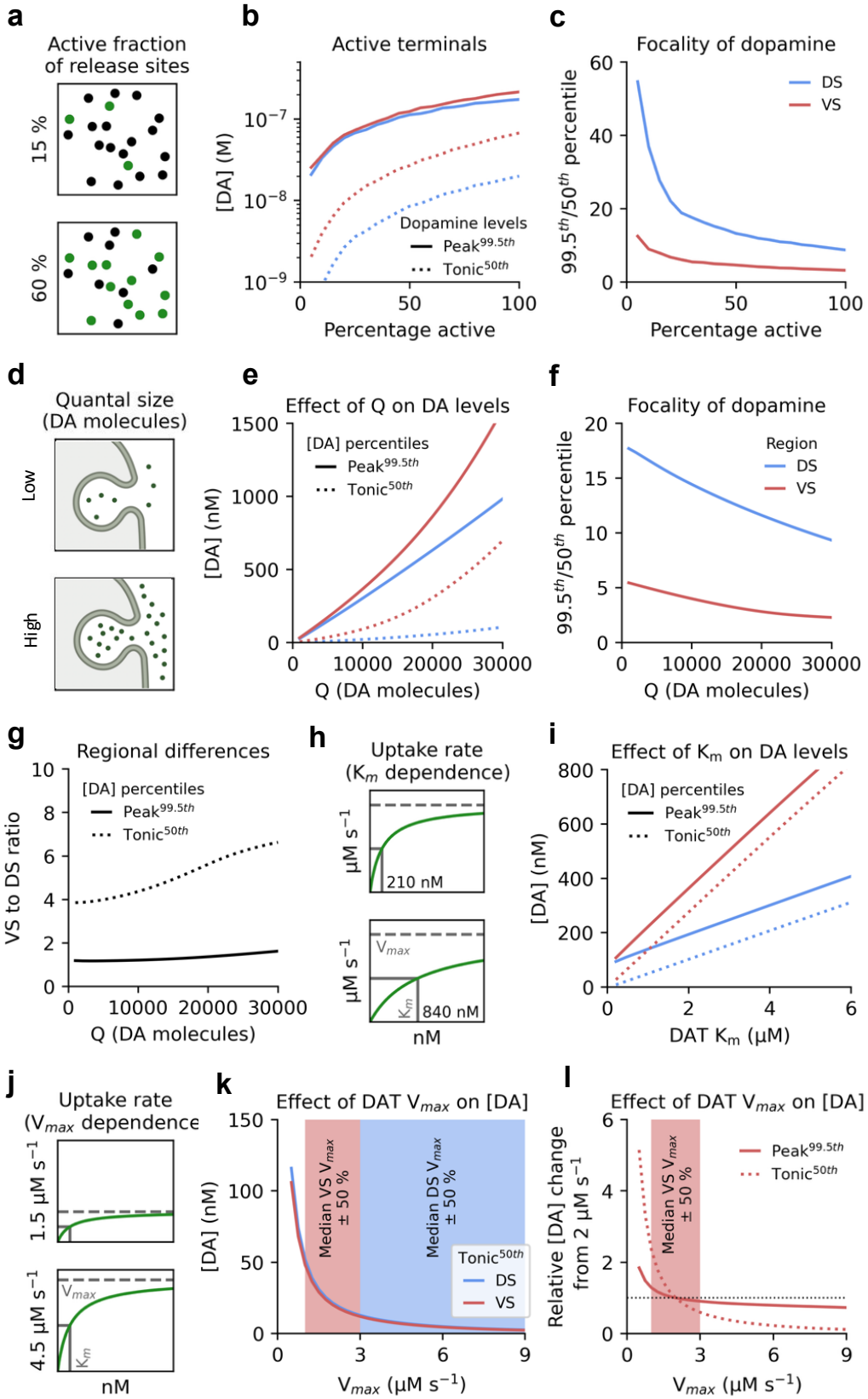

Figure 3. Sensitivity of the model to parameter changes. (**a**) Schematic of the fraction of active release sites. Black dots are inactive sites and green dots indicate actively releasing

997 sites. (**b**) Effect of changing fraction of active release sites on DA concentrations. Blue line,
998 DS peak DA concentration (99.5th percentile); Red line, VS peak DA concentration (99.5th
999 percentile); Dotted blue line, DS tonic DA concentration (50th percentile); Dotted red line, VS
1000 tonic DA concentration (50th percentile). (**c**) Ratio between peak (99.5th percentile) and tonic
1001 (50th percentile) concentrations across fractions of active release sites in the DS (blue line)
1002 and VS (red line) as a measure of DA signal focality. (**d**) Schematic of changing quantal size
1003 (Q). (**e**) Effect of changing quantal size on tonic and peak DA concentrations in DS (blue
1004 lines) and VS (red lines). (**f**) Ratio between peak and tonic concentrations across various
1005 quantal sizes in in DS (blue line) and VS (red line). (**g**) Relative difference between the DS
1006 and VS for peak (black line) and tonic DA (dotted line) at different quantal sizes. (**h**)
1007 Schematic of changing DAT K_m. (**i**) Effect of changing DAT K_m on DA concentrations in DS
1008 (blue lines) and VS (red lines). **j,** Schematic of changing DAT V_{max}. (**k**) Effect of changing DAT
1009 V_{max} on DA concentrations. Shaded areas are median V_{max} of the two regions (DS and VS) as
1010 found in the literature shown in Table S2 ± 50%. (**l**) Effect of changing DAT V_{max}, with tonic
1011 (50th percentile) and peak (99.5th percentile) DA concentrations normalized to their value at
1012 2 µm s^{-1} (median value for VS). Shaded area indicates median V_{max} for VS found in the
1013 literature shown in Table S2 ± 50%.
1014

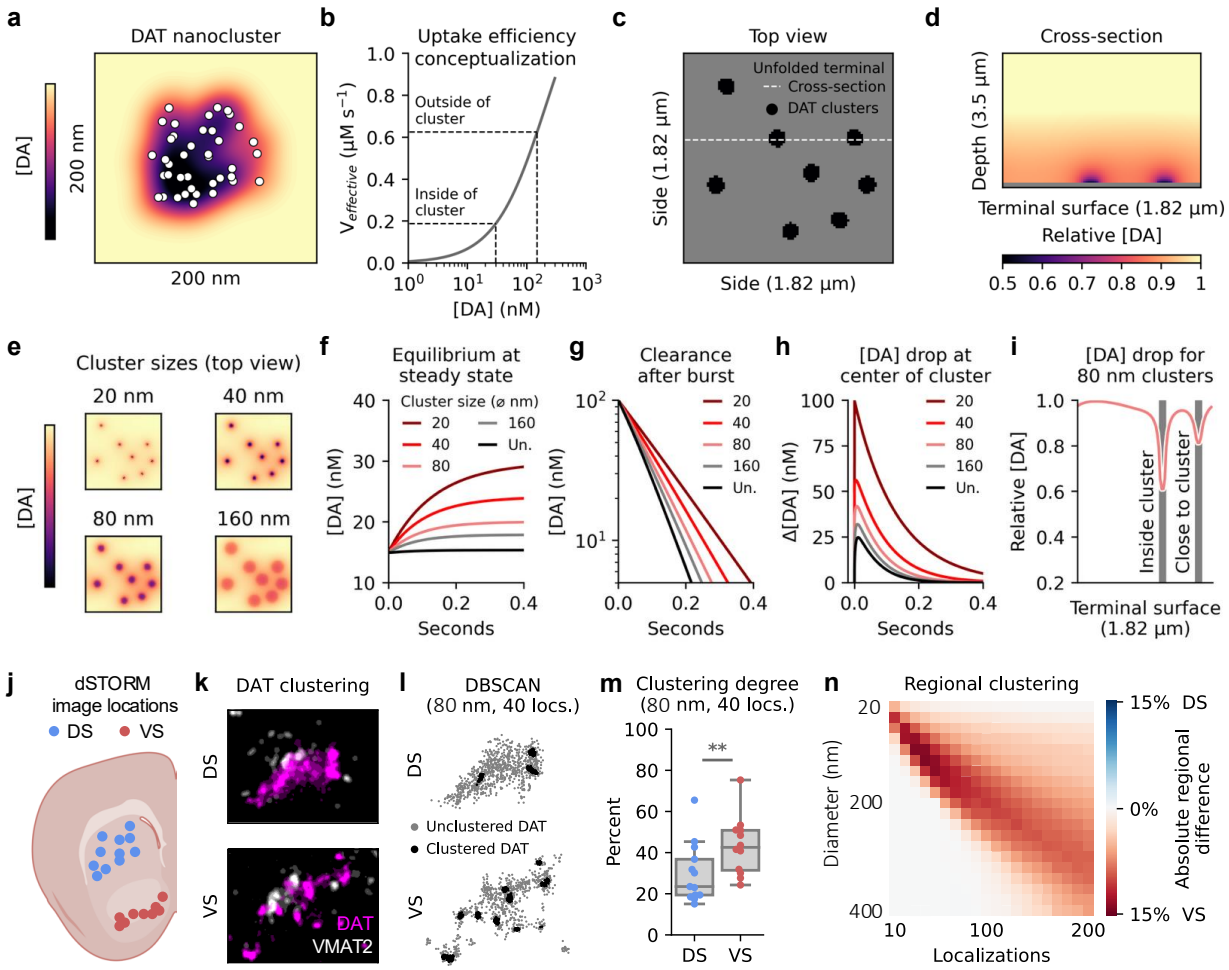

Figure 4. DAT nanoclustering reduces uptake and shows regional variation. (**a**) Schematic of dense DA cluster. White dots represent individual DAT molecules, and colour gradient the surrounding DA concentration. (**b**) Effective transport rate dependent on local concentration. (**c**) Top view of unfolded DA varicosity. Black shapes denote clusters of DAT. Dashed white line indicates placement of cross-section shown in (d). (**d**) Cross section showing DA concentration in space surrounding varicosity unfolded in c. Grey line at the bottom is surface of the varicosity. Colour-coded for DA concentration. (**e**) Top view from (c), but colour coded for DA concentration immediately above membrane surface at different DAT cluster sizes. (**f**) Changes in [DA] from 15 nM unclustered (Un.) steady state with constant release after changing to four different cluster size scenarios (ø = diameter). (**g**) Clearance of 100 nM [DA] for different DAT cluster sizes. (**h**) Difference between DA concentration at the centre of clusters (or general surface of varicosity for unclustered) and mean concentration of the full simulation space (**i**) Concentrations across a cross section of a surface with 80 nm diameter clusters. Shaded areas highlight cluster locations. (**j**) Location of images of the dorsal (DS) and ventral striatum (VS) in striatal slices from mice as imaged in *(Sorensen et al., 2021)* with direct stochastic optical reconstruction microscopy (dSTORM). (**k**) Two representative DA varicosities from DS and VS with VMAT2 in white and DAT in magenta. Images are 1.5x2 µm. (**l**) Individual DAT localizations (locs.) from images in (k) coloured by clustering. Black indicates localization identified as clustered based on DBSCAN with parameters 80 nm diameter and 40 localizations. Grey indicates unclustered localizations. (**m**) Quantification of clustering across all images in (j) with parameters in (l).

Welch's two-sample t-test, P = 0.012(*), n = 12 (DS) and 13 (VS). (**n**) Absolute difference in percentage of clustering as assessed with DBSCAN across a range of parameters. VS has a higher propensity to cluster across cluster sizes typically reported for DAT clusters.